Inorganic Chemistry
Cite This: Inorg. Chem. XXXX, XXX, XXX−XXX
Article
pubs.acs.org/IC

Serendipitous Assembly of Mixed Phase $BiVO_4$ on B-Doped g-C_3N_4: An Appropriate p−n Heterojunction for Photocatalytic O_2 evolution and Cr(VI) reduction

Pradeepta Babu, Satyaranjan Mohanty, Brundabana Naik,* and Kulamani Parida*

Centre for Nanoscience and Nanotechnology, Siksha 'O' Anusandhan, Bhubaneswar 751030, India

Supporting Information

ABSTRACT: Type II p−n heterojunction B-doped g-C_3N_4/$BiVO_4$ moieties have been fabricated by depositing n-type $BiVO_4$ on the surface of p-type 1 wt % B-doped g-C_3N_4 for the first time. The materials were characterized by PXRD, XPS, UV−vis DRS, IR, PL, and Raman analysis. The photocatalytic activities of as synthesized samples were studied toward reduction of Cr(VI) and water splitting reaction to generate oxygen. The results reveal that Type II p−n heterojunction considerably enhance the photocatalytic activity as compared to neat n-type $BiVO_4$ and p-type B-doped g-C_3N_4. 50% $BiVO_4$/B-doped g-C_3N_4 heterostructure exhibited the best photocatalytic activity, which is 7.9-fold higher than that of $BiVO_4$ and followed by a pseudo first order kinetics with apparent first order rate constant of 0.063 min^{-1}. Again the heterojunction is able to produce 4.2 times higher oxygen evolution value as related to pristine $BiVO_4$. The superior photocatalytic activity is attributed to higher visible light utilization and lower recombination of electron−hole pairs by creating a p−n junction. PXRD and HRTEM data suggest the formation of mixed phase monoclinic and tetragonal $BiVO_4$ thereby creating a heterojunction for the improvement of the photocatalytic performances. The formation of mixed-phase $BiVO_4$ is attributed to the high temperature calcination as well as surface energy of B-doped g-C_3N_4. The oxygen vacancy in the system is confirmed through XPS and Raman analysis. Moreover, the excellent photocurrent response by the designed photocatalyst at lower overpotential and decrease in carrier recombination as compared to bulk one, studied from LSV and electrochemical impedance spectroscopy, validate the unique photocatalytic activity of the catalyst. The formation of the p−n heterojunction is confirmed from a Mott−Schottky analysis. The work shed new light on the assembly of the p−n heterojunction, showing excellent photocatalytic properties in a simple way.

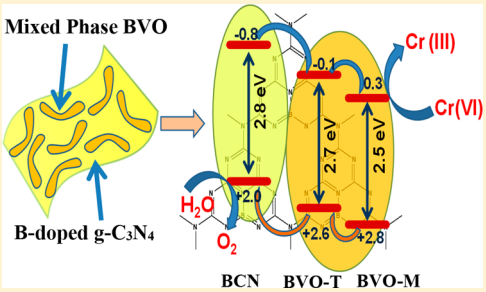

INTRODUCTION

Since the photocatalytic process is regarded worldwide as a preeminent method to resolve the extreme problems of energy deficiency and environmental crisis, the design of a visible light active photocatalyst has been gaining more attention.[1,2] Semiconductor photocatalysis is a cutting-edge technology which can convert solar energy to chemical energy that could be used for removal of pollutant and various chemical transformation processes including water oxidation to generate O_2.[3,4] TiO_2 has become a model photocatalyst due to its nontoxicity, higher stability, and tremendous oxidizing ability. However, due to its wide band gap characteristics, the catalyst is able to absorb only ultraviolet light, which covers only 4% of solar energy.[5] Moreover, the high density of the trap state, which leads to fast electron−hole recombination process, supplements another limitation of TiO_2. Hence, catalyst design including visible light active catalyst is one of the most promising tasks in the current scenario of research.[6,7] In this context, $BiVO_4$[8,9] has drawn great attention as a visible light responsive catalyst due to its narrower band gap, good photostability, nontoxicity, and higher sunlight utilization ability. Nevertheless, the valence band of $BiVO_4$ is sufficiently positive and acts as a photoanode that facilitates the oxygen evolution reaction. Generally, $BiVO_4$ exists in three different polymeric forms,[10] i.e., zircon-tetragonal, scheelite-tetragonal, and scheelite-monoclinic. Among these, the monoclinic phase[11] is the most interesting one due to its higher photocatalytic activity as compared to both tetragonal phases. The reason for this is due to the high band gap of tetragonal phase possessing an UV absorption band (2.9 eV) as compared to monoclinic system (2.4 eV) having both an UV and visible absorption band. The transition of the electron from O 2p to V 3d is responsible for generation of the UV band. The visible light band is assigned to the movement of electrons from the valence band[12] (available from hybrid orbital of Bi 6s and O 2p) to the conduction band (formed by V 3d orbital). Again separation efficacy of electron and hole pair is improved in case of monoclinic $BiVO_4$ due to the distortion of Bi−O bond. Further DFT calculation demonstrate that hole mobility[13] is an important parameter for the enhanced photocatalytic activity by monoclinic phase compared to tetragonal analogue. However, the bulk monoclinic $BiVO_4$ suffers from lower

Received: July 30, 2019

Downloaded via STOCKHOLM UNIV on August 28, 2019 at 15:31:25 (UTC).
See https://pubs.acs.org/sharingguidelines for options on how to legitimately share published articles.

© XXXX American Chemical Society

DOI: 10.1021/acs.inorgchem.9b02309
Inorg. Chem. XXXX, XXX, XXX−XXX

activity due to poor charge transfer[14] properties and weak surface adsorption characteristics.

Various strategies have been demonstrated so as to develop the photocatalytic property of monoclinic $BiVO_4$, including heterojunction construction,[15] loading of cocatalyst,[16] and doping of impurity[17] to its lattice structure. Of these approaches, the construction of heterojunction with different crystalline phases[18] of $BiVO_4$ appears to be a new way. The heterojunction between phases generally have a higher interfacial charge transfer rate[19] and can be easily synthesized by adjusting the pH of the reaction medium[20] or controlling the heating temperature[18] during the crystallization process. Tan et al. has shown that the coexistence of a mixed phase structure has enhanced photocatalytic behavior toward RhB degradation.[20] Fan et al. has confirmed that the interface of monoclinic and tetragonal phase provides a suitable path for separation of photoinduced electrons[19] and also changes their direction of migration. Cheng et al. has synthesized $BiVO_4$ nanofibers by an electrospinning method[18] with controlled heat treatment. The improved photocatalytic activity toward RhB degradation was due to the formation of phase junction between the tetragonal and monoclinic phase. The existence of heterostructured material obviously leads to the enhanced charge separation and migration thereof, thereby improving the photocatalytic process.

Carbon materials such as graphitic carbon nitride[21] (g-C_3N_4) belongs to an important class of material in the domain of photocatalytic research owing to its unparalleled capability to utilize visible light and brilliant chemical and thermal strengths. The material consists of tris(s-triazine) repeating groups which are responsible for the good electrical conductivity due to high electron mobility.[22] The catalyst can easily be synthesized on a large scale just by heating simple organic molecules like urea and melamine. The polymer has a moderate band gap of 2.7 eV, which absorbs visible light of the solar spectrum.[23,24] However, bulk g-C_3N_4 has a low specific surface area and also possesses fast electron−hole recombination due to the $\pi-\pi$ stacking among the aromatic layers. Recently, numerous approaches have been demonstrated to improve its photocatalytic property including the design of nanostructured array,[25−27] heterojunction construction,[28,29] and impurity doping[23,30] to its lattice structure. Doping of metal[31] or nonmetal[32] into the g-C_3N_4 lattice may able to tune the valence and conduction band edge potential, enhancing higher photocatalytic activity. In this context, boron doping[23,33] is important because it not only alters the conductivity of g-C_3N_4 from n- to p-type but also shifts its conduction band negative enough to facilitate various reduction reactions including chromium reduction and hydrogen evolution reaction. Again, heterojunction photocatalysts constructed on g-C_3N_4 have been extensively designed to minimize the fast charge recombination of the polymer. In this perspective, Li et al. has constructed a monoclinic porous $BiVO_4$/g-C_3N_4 nanocomposite that shows excellent photocatalytic activity toward RhB degradation.[34] Samanta et al. has designed the $BiVO_4$/g-C_3N_4 heterostructure for the oxidation of aromatic alcohols with improved selectivity.[35] Coral-like direct Z-scheme $BiVO_4$/g-C_3N_4 has been synthesized by Sun et al. for photocatalytic oxidation of toluene.[36] Wang et al. has combined the electrospinning preparation of a $BiVO_4$/g-C_3N_4 composite film and explored its photoelectrochemical performances.[37] The g-C_3N_4 nanosheet not only forms a heterojunction but also prevents the agglomeration of $BiVO_4$. Considering modified g-C_3N_4, Kong et al. has synthesized S-doped C_3N_4/$BiVO_4$ composite via impregnated coprecipitation method.[38] The nanocomposite shows 129 and 349% enhancement in water oxidation and charge carrier lifetime, respectively, as compared to pristine $BiVO_4$. Hou Yang et al. have synthesized polymeric carbon nitride foam and explored its photocatalytic activity toward tetracycline removal in different natural water matrices including wastewater and natural water. Yan Wu et al. have demonstrated a Z-scheme-based 2D−2D heterostructure consisting of oxygen-doped carbon nitride and ultrathin Co−Al layered double hydroxide and tested its photocatalytic activity toward MO degradation. Again the group has synthesized petal-like CdS nanostructures coated with S-doped graphitic carbon nitride, which shows excellent activity toward RhB degradation and H_2 evolution. Yan Wu et al. have demonstrated hierarchical 2D-2D $Zn_3In_2S_6$/ fluorinated carbon nitride nanosheet for boosting photocatalytic MO degradation and H_2 evolution. Again the same group has constructed a Z-scheme-based p−n heterojunction by coupling $LaFeO_3$/g-C_3N_4 for Brilliant Blue degradation.[39−43]

This work demonstrates the construction of a novel and efficient heterojunction catalyst with mixed phase Bi-VO_4(monoclinic-tetragonal) decorated on B-doped graphitic carbon nitride nanosheet for the first time. BVCN were synthesized by a facile impregnated coprecipitation method followed by calcination. As synthesized catalysts were tested for photocatalytic water oxidation and chromium reduction and show excellent catalytic activity compared to pristine $BiVO_4$. The synthesis, characterization, and photocatalytic properties of the catalysts were discussed in detail.

EXPERIMENTAL SECTION

Materials. Bismuth nitrate, ammonium vanadate, melamine, boric acid, silver nitrate, and potassium dichromate were purchased from Merck. All chemicals were used as received without any further purification. Double distilled water is used throughout all experiments.

Synthesis of B-Doped g-C_3N_4(BCN). B-doped g-C_3N_4 (1 wt %) was synthesized via the reported procedure with slight modification.[23] A 10 g sample of melamine and 0.572 g of boric acid were taken in 300 mL of water and heated at 80 °C for 12 h whereupon a white crystalline compound is formed. The as obtained compound was calcined at 550 °C for 2 h and calcined at 450 °C for 1 h to give a light yellow color powder.

Synthesis of Monoclinic $BiVO_4$(BVOM). First, 6 g of bismuth nitrate was put in 100 mL of water, and 0.8 mL of nitric acid was added into it. The whole solution was stirred for 30 min. In another beaker, 1.4 g of ammonium vanadate was added into 100 mL of water and the mixture stirred to give a yellow solution. Then the above solution was added dropwise to bismuth nitrate solution to give an orange color precipitate. After 30 min of continuous stirring, the pH of the solution was neutralized to 7 by addition of ammonium hydroxide solution. The light yellow color precipitate was filtered and dried to give the desired compound.[44] Tetragonal $BiVO_4$ was also synthesized by following literature procedures[45] described elsewhere (BVOT). Mixed phase $BiVO_4$ (BVOMT) was synthesized by calcining as synthesized BVO at 400 °C.

Synthesis of $BiVO_4$−B Doped g-C_3N_4 (BVCN). First, 0.73 g of bismuth nitrate and 1 g of B-doped g-C_3N_4 were taken into 200 mL of water and sonicated for 30 min and stirred. To the above solution was added 0.5 mL of nitric acid, and stirring was continued for 1 h. In another beaker, 0.175 g of ammonium vanadate was dissolved in 20 mL of water, the yellow colored solution was added dropwise to the above solution, and stirring was continued for 30 min. Finally the pH of the solution was neutralized by adding ammonium hydroxide and the light yellow color precipitate was filtered, dried and calcined at

DOI: 10.1021/acs.inorgchem.9b02309
Inorg. Chem. XXXX, XXX, XXX−XXX

Scheme 1. Formation of $BiVO_4$–B-Doped g-C_3N_4 p–n Heterojunction

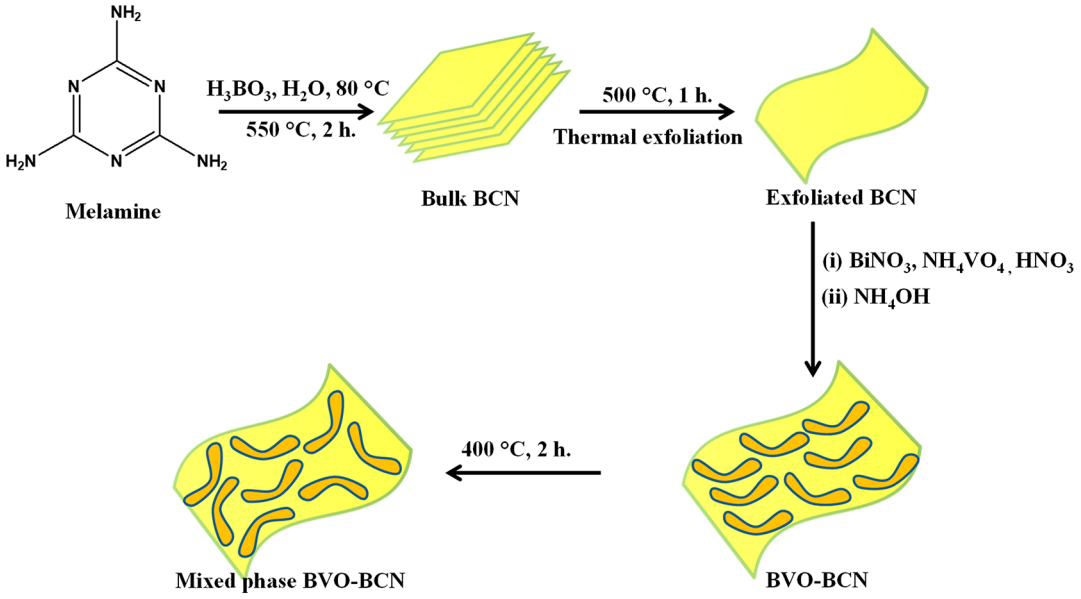

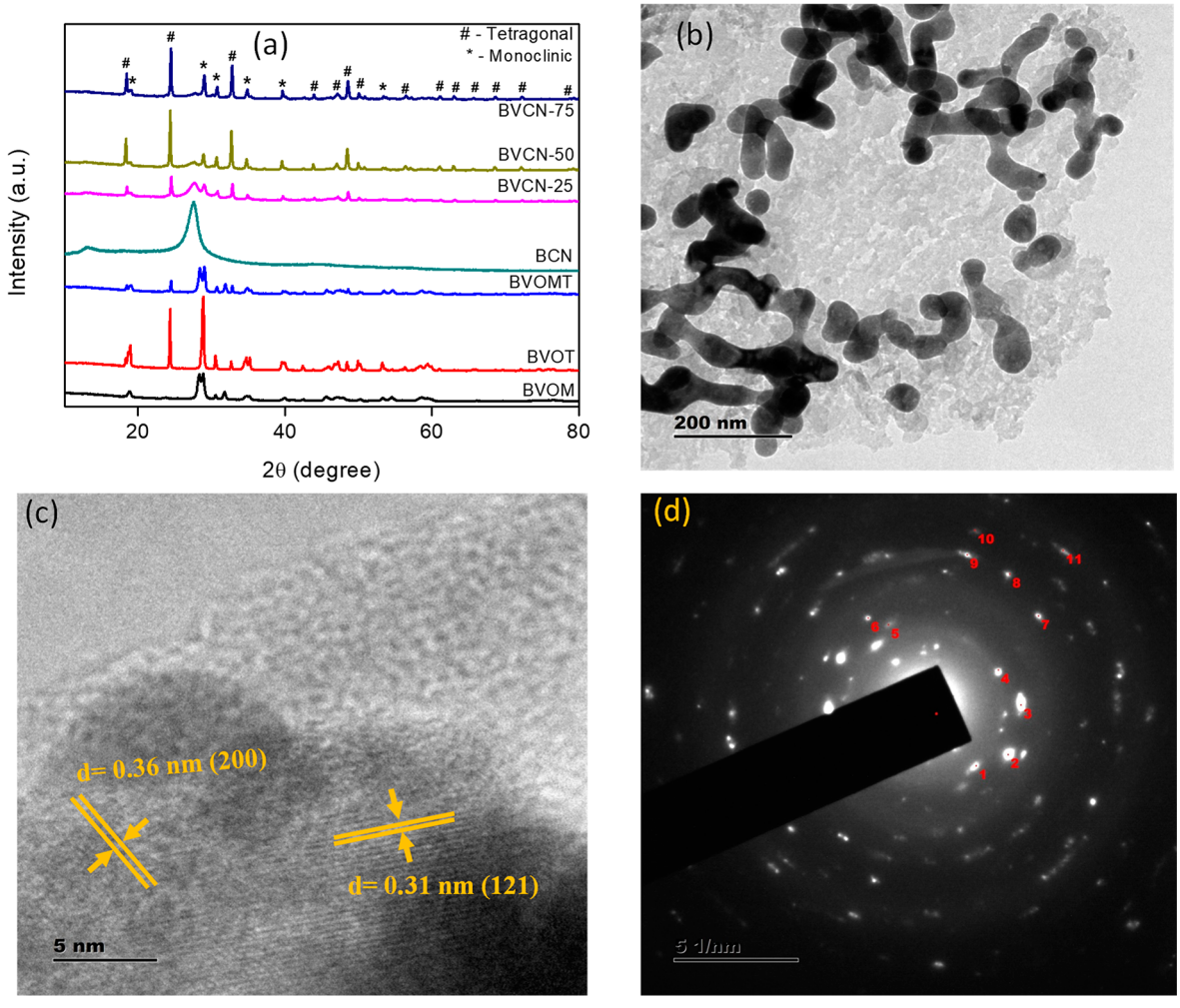

Figure 1. (a) PXRD of as synthesized material showing mixed phase BVO in BVCN. (b) HRTEM images of BVCN where cashew nut shape BVO is dispersed in BCN nanosheet. (c) Lattice fringe width of BVCN matching with *d* values of both monoclinic and tetragonal phase of BVO. (d) SAED pattern of BVCN.

DOI: 10.1021/acs.inorgchem.9b02309
Inorg. Chem. XXXX, XXX, XXX–XXX

400 °C to get BVCN-50. BVCN-25 and BVCN-75 were synthesized by following the same procedure by varying the weight percent of $BiVO_4$ precursor (Scheme.1).

Photocatalytic Water Oxidation and Cr(VI) Reduction. The properties of as synthesized photocatalysts were assessed through photocatalytic water oxidation and Cr(VI) reduction reaction upon visible light illumination. Photocatalytic water splitting reaction for oxygen generation was done in a 100 mL sealed quartz batch reactor fitted with a 150 W xenon lamp having a 420 nm cut off filter. Typically 20 mg of catalyst was spread in a 20 mL solution (5 mmol $AgNO_3$). $AgNO_3$ is used as electron acceptor[46] from the semiconductor photocatalyst and provided the hole for the water oxidation reaction. Proper dispersion of photocatalyst was achieved by stirring the solution with a magnetic stirrer, and the dissolved gases were removed by passing nitrogen gas a number of times over the reaction medium before light illumination. The experiment was performed at room temperature by circulating cold water, and developed gas was accumulated by downward displacement of water. Analysis of the collected gas was done via a gas chromatograph equipped with a 5 Å molecular sieve column with a thermal conductivity detector built-in and confirmed as oxygen. For photocatalytic Cr(VI) reduction, 50 mg of each catalyst was put in a 100 mL Pyrex glass containing 20 mL of Cr(VI) solution (20 mg L^{-1}). Before light irradiation, the suspension was magnetically stirred for 30 min to confirm the establishment of adsorption/desorption equilibrium. Visible light was illuminated by using a 150 W xenon lamp fitted with a cutoff filter ($\lambda > 420$ nm). By circulating cold water, the temperature of the reaction solution was maintained at room temperature. During illumination, 2 mL of solution was extracted through a syringe at given time interval and centrifuged to remove the catalyst. The conversion of Cr(VI) to Cr(III) was monitored colorimetrically by using diphenylcarbazide (DPC) method[47] where absorbance maximum is observed at 545 nm.

CHARACTERIZATION

X-ray diffraction patterns of as synthesized materials were recorded in the 2θ range 10−80° with a scan rate of 2° min^{-1} on a Rigaku miniflex diffractometer equipped with Cu Kα radiation (λ = 1.45 Å). High resolution transmission electron microscopy (JEOL-JEM 2010, Japan) obtained with an energy dispersive X-ray spectrometer (Oxford Instrument, INCA, U.K.) was used for the structure and morphology determination of the materials. X-ray photoelectron spectroscopy (XPS) was done in a XPS system in a Krato Axis 165 instrument equipped with a Mg Kα source. DRUV spectra and photoluminescence (PL) spectra were carried out on JASCO UV−vis spectrophotometer and JASCO-FP-8300 spectrofluorometer, respectively. JASCO-FT-IR-4600 spectrometer was used to record the IR spectra of synthesized material taking KBr as reference and frequency range was set from 400 to 4000 cm^{-1}. Electrochemical experiments were performed using a IVIUMnSTAT instrument where Pt and Ag/AgCl electrodes were taken as counter and reference electrodes, respectively. The electrophoretic deposition method has been taken into consideration for preparation of the working electrode. Typically 30 mg of catalyst and iodine were taken in 30 mL of acetone, and proper dispersion of catalyst was done by a sonicating the solution for 10 min. Two parallel fluorine doped tin oxide (FTO), separated with 15−20 mm distances, were immersed in the above solution, and 60 V bias was set for 3 min to deposit the catalyst on the FTO surface. The FTOs were calcined at 200 °C for 2 h to remove the impurities on the surface of the catalyst. The linear sweep voltammetry (LSV) was performed through applying the potential from 0.4 to 1.3 V (scan rate 25 mV/s) and illuminated with a 300 W xenon lamp. Electrochemical impedance spectroscopy (EIS) was performed at zero biased potential in the dark and with the range of frequency set from 10^{-2} to 10^{5}. All electrochemical experiments were carried out in 0.2 M Na_2SO_4 solution.

RESULTS AND DISCUSSION

Crystal Structure. The crystal structure, phase purity, and composition of as prepared catalyst were analyzed by powder XRD.[48] As shown in Figure 1a two pronounced peaks at 2θ = 13.2° and 27.6° were observed for BCN which are indexed to 100 and 002 planes of graphitic carbon nitride.[49,23] The 100 peak is attributed to stacked conjugated aromatic ring and 002 planes represent the in plane structural packing of triazine group. The well-known three polymorphs of $BiVO_4$ are zircon structure with tetragonal system (z-t) and scheelite structure with monoclinic (s-m) and tetragonal (s-t) systems.[10] The pure BVO shows a series of sharp and narrow diffraction peaks which is the well-known monoclinic phase (JCPDS-00−014−0688, space group $I2/a$) of bismuth vanadate with cell constant a = 5.195, b = 11.701, c = 5.092. BVO exhibits peaks at 18.9°, 28.4°, 28.8°, 30.5°, 34.8°, 39.9°, 40.7°, 42.4°, 45.6°, 47.6°, 50.2°, 53.2°, 54.4°, 58.6°, and 59.2° which are assigned to (011), (−130), (−121), (040), (200), (211), (112), (051), (231), (042), (202), (−161), (013), (321), and (123), respectively. Interestingly in case of heterojunction such as BVCN-25, BVCN-50, and BVCN-75, a peak at 24.3° is observed which is attributed to zircon tetragonal phase[50] of BVO (JCPDS-00-014-0133, space group $I41/amd$) with cell constant a = 7.299, b = 7.299, c = 6.457. The percentage of monoclinic phase[51] in BVCN heterostructure is calculated by using the following equation.

$$\eta_{mono} = \frac{I_{mono(121)}}{I_{mono(121)} + I_{tetra(200)}} \times 100$$

Here η_{mono}, $I_{mono(121)}$, and $I_{mono(200)}$ represent the percentage of monoclinic phase in mixed phase BVO, the relative intensity of (121) peak for monoclinic phase, and the (200) peak for the tetrahedral phase, in that order. The calculated η_{mono} were found to be 66, 30.9, 17.4, and 29.2% for BVOMT, BVCN-25, BVCN-50, and BVCN-75 respectively. The experiments were repeated for three times and it was found that the decrease in percentage of monoclinic phase in BVCN composite is attributed to the surface energy of BCN. Here surface energy plays a pivotal role in creating the crystal structure of certain phase. The interfacial interaction between functionalized graphene[52] sheets and metal oxide nanoparticles is believed to control the nucleation energy for different phases of TiO_2. So we assume that the free amino group ($-NH_2$) present on the edge of g-C_3N_4 will interact strongly to the Bi^{3+} and controlled the growth of lattice by forming mixed phase BVO. Again due to the high temperature calcination of the material BVCN, few of the B could be inserted into BVO lattice during the nucleation process, which is responsible for the formation of mixed phase BVO. The assumption correlates to the formation of noisy peak in XPS spectrum of B 1s from 188 to 196 eV which relates to the B−N coordination *vide infra*. Again crystallite size of as synthesized samples were calculated using Scherrer's equation[53] and found to be 15.9, 50.3, 29.8, 4.6, 27.5, 36.4, and 37.3 nm for BVOM, BVOT, BVOMT, BCN, BVCN-25, BVCN-50, and BVCN-75, in that order. FT-IR were obtained in order to explore the molecular structure[54] of the as synthesized materials. Analogous to BCN, the additional heterostructures have prominent vibration peak of triazine unit around 800 cm^{-1} and stretching mode of aromatic heterocycles[23] around 1200−1600 cm^{-1} (Figure S1a). The peak around 990, 825, and 733 cm^{-1} links to the symmetric and asymmetric stretching vibrations of V−O bond. The band around 530 cm^{-1} is attributed to the stretching vibration of Bi−O bond. The peaks from 3000 to 3600 cm^{-1} links to the stretching mode of vibration of $-NH_2$ and −OH groups

DOI: 10.1021/acs.inorgchem.9b02309
Inorg. Chem. XXXX, XXX, XXX−XXX

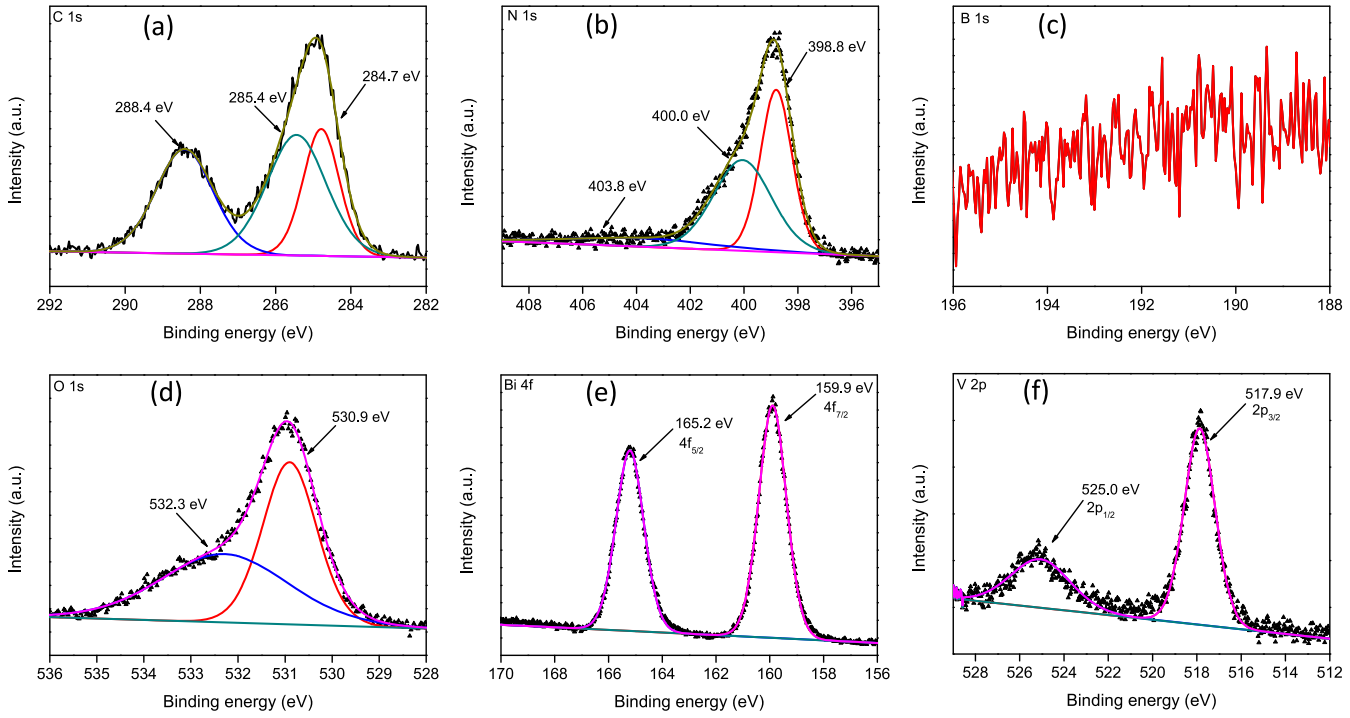

Figure 2. XPS spectra of BVCN (a) C 1s, (b) N 1s, (c) B 1s, (d) O 1s, (e) Bi 4f, (f) V 2p.

having hydrogen bonding. Again Raman spectroscopy[55,56] has been conducted in order to elucidate the structure and bonding of the constituents of heterostructure through their characteristic vibration and shown in Figure S1b. The monoclinic phase of BVOM[57,58] exhibits five noticeable peaks at 829.6, 734.9, 342.0, 223.3, and 130.3 cm^{-1} which are attributed to the vibrational features of VO_4 tetrahedron.[59] The intense peak at 829.6 cm^{-1} and weak peak at 734.9 cm^{-1} are assigned to the shorter symmetric and long asymmetric V−O stretching mode of vibration with A_g and B_g symmetry in that order. The peak present at 341.3 cm^{-1} resembles to asymmetric bending vibration of the VO_4 tetrahedron. The external mode including rotation/vibration of BVO is assigned to the peaks at 223.3 and 130.3 cm^{-1}. Interestingly the peak at 829.6 cm^{-1} has been shifted to lower frequency[60] in case of composite and is ascribed at 828.0, 825.0, and 828.7 cm^{-1} for BVCN-25, BVCN-50, and BVCN-75 respectively. Such results correspond to the elongation of V−O bond leading to structural distortion which occurs due to the modification of electronic band structure of BVOM in the heterostructure. The shifting of symmetric stretching mode of vibration to a lower frequency is more in case of BVCN-50 and intensity also decreases to a larger extent indicating that high degree of crystallinity and oxygen vacancy in the system. This result can be corroborated with PXRD and XPS analysis and links to the higher photocatalytic activity by BVCN-50 as compared to other synthesized catalysts.

Morphology Study. High resolution transmission electron microscopy (HRTEM) has been done so as to appreciate the morphological[61] as well as crystalline[62] nature of the photocatalyst. The Figure 1b reveals the formation of cashew nut shaped BVOs which are well dispersed on BCN nanosheet. The dark and light gray area in TEM images represents BVO and BCN respectively. The BCN not only acts as support but also restricts the agglomeration of BVO that relates to the extraordinary photocatalytic activity of the materials. Again the lattice fringes with *d* spacing value 0.31 and 0.36 nm are attributed to the (121) and (200) lattice planes of both monoclinic and tetragonal phase of BVO shown in Figure 1c. The polycrystalline nature of the material is yet again confirmed from selected area electron diffraction (SAED) pattern of BVCN which consists of numbers of diffraction rings (Figure 1d). The concentric rings are assigned as 1, 2, 3, 4, 5, 6, 7, 8, and 9 which represent (200), (121), (211), (002), (051), (213), (420), (123), and (224) lattice planes of BVCN as revealed from Figure 1d. The (200), (211), (213),(420), and (224) planes represent the tetragonal phase and (121), (051), and (123) link to the monoclinic phase of BVO whereas the (002) crystal plane stands for BCN. The TEM observation confirmed the formation of a tight heterojunction between the mixed phase BVO and BCN in BVCN and the existence of both monoclinic and tetragonal phase of BVO, which is in accordance with PXRD data. FESEM were performed in order to explore the morphology of BVO, BCN, and BVCN-50. From the Figure S2 it is clear that spherical shape BVOM (Figure S2a) has been formed where as in case of BCN (Figure S2c), crumpled nanosheet with worm-hole mesoporosity is present. When spherical BVO is deposited on to the BCN nanosheet, wrapping of nanosheet takes place to form BVCN-50 (Figure S2e) p−n heterojunction. The EDX spectra show the successful formation of BVO, BCN and BVCN-50 (Figure S2, parts b, d, and f). Elemental mapping shows the uniform distribution of constituent atoms of BVCN-50 (Figure S3). Further, In order to relate the surface area with the photocatalytic activity of the photocatalysts, nitrogen adsorption−desorption isotherm has been performed for BVO-MT, BCN and BVCN-50. From the Figure S4, it is revealed that all photocatalysts show type-IV isotherm according to BDDT classification, which relates to the presence of mesopores with 2−50 nm. The H3 type hysteresis loop suggested the formation of worm-hole mesoporosity, which links to the excellent photocatalytic activity by the photocatalyst. The pore

DOI: 10.1021/acs.inorgchem.9b02309
Inorg. Chem. XXXX, XXX, XXX−XXX

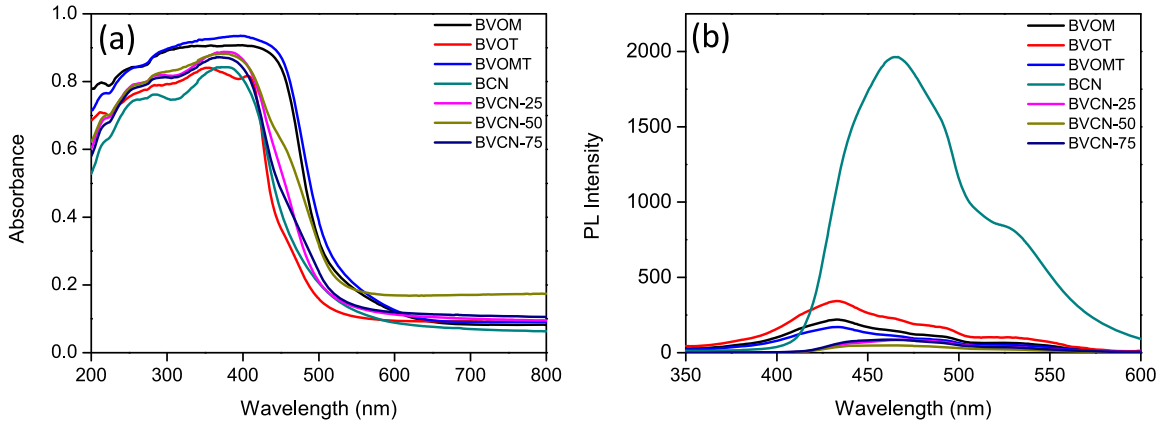

Figure 3. (a) UV−vis spectra and (b) photoluminescence spectra of BVOM, BVOT, BVOMT, BCN, BVCN-25, BVCN-50, and BVCN-75.

volume of BVO-MT, BCN, and BCN-50 was found to be 0.0316, 0.0635, and 0.0655 cm^3/g. The specific surface area of BVO-MT, BCN, and BVCN-50 were 7.62, 10.55, and 19.76 m^2/g. The excellent photocatalytic activity of BVCN-50 for O_2 evolution and Cr(VI) reduction may be due to its highest surface area.

X-ray Photoelectron Spectroscopy. To explore the surface elemental composition and chemical status of as synthesized photocatalyst, X-ray photoelectron spectroscopy[23,63] measurement has been carried out. The XPS survey spectra of photocatalyst consists of Bi, V, O, C, N, and B elements, the primary constituents of the photocatalyst. The C 1s, Bi 4f, V 2p, O 1s, N 1s, and B 1s core-level could be easily observed in the XPS survey spectra (Figure S5f). Additionally the chemical statuses of the elements were analyzed by their analogous high resolution XPS spectra and fitted by means of CASA. The peak positions of all the XPS spectra were calibrated with C 1s with 284.7 eV. High resolution C 1s core (Figure 2a) of BVCN consist of three distinct peaks at 284.7, 285.4, and 288.4 eV that are attributed to carbide, unintended carbon species[64] from the XPS instrument itself, and sp^2-hybridized carbon attached to nitrogen of the aromatic ring (N−C═N) of g-C_3N_4 framework respectively. Similarly in case of N 1s (Figure 2b) the peak present at 398.8 eV is ascribed to nitride or cyanide (N^{3-} or −C≡N).[38,65] The peak at 400.0 eV corresponds to the sp^2 hybridized nitrogen attached to a carbon atom (C═N−C) and the peak at 403.8 eV associate with the tertiary nitrogen relates to N−$(C)_3$ group existing in the aromatic ring of carbon nitride. The core level of B 1s (Figure 2c) was found to be noisy due to its low atomic percent doping in carbon nitride.[23] To confirm the successful boron doping, XPS spectra of neat BCN has been done and represented in Figure S5a−e. High resolution O 1s XPS spectrum (Figure 2d) of BVCN has 2 peaks positioned at 530.9, 532.3 eV corresponds to the V−O bond and oxygen vacancy[60,66] in BVO lattice respectively. The O 1s peak at 532.3 eV is related to oxygen vacancy in crystal lattice due to high temperature calcination of the material. The core level of Bi 4f[55,67] (Figure 2e) spectrum shows two peaks having binding energy at 159.9 and 165.2 eV which corresponds to Bi $4f_{7/2}$ and Bi $4f_{5/2}$ in that order. Similarly V 2p core level (Figure 2f) XPS spectrum is fitted into two characteristics peaks, positioned at 517.9 and 525.0 eV link to V $2p_{3/2}$ and V $2p_{1/2}$ in that order.

Optical Properties. The photophysical[68] characteristics of all photocatalysts were studied using UV-DRS and photoluminescence spectroscopy. From the Figure 3a, it is clear that all photocatalysts were able toward absorption of visible light of solar spectrum. It is interesting to note that BVCN-50 has more absorption tail as compared to other photocatalysts. BCN, BVOM, BVOT, BVOMT BVCN-25, BVCN-50, and BVCN-75 absorb visible light with onset potential of 430, 530, 458, 534, 544, 600, and 551 nm. Upon light illumination, electrons of BVO are excited from the valence band containing O 2p into the conduction band of V 3d orbitals.[69] The enhancement in the absorption tail of BVCN-50 suggests it to be the foremost photocatalyst compared to all. Furthermore, the band gap of the as synthesized materials was calculated using Tauc's plot (Figure S6a).[23]

$$\alpha h\nu = A(h\nu - Eg)^n$$

Here α stands for the absorption coefficient, ν is the frequency of light, A is proportionality constant and E_g links to the band gap energy. The value of n in Tauc's equation relates to the kind of transition in semiconductor photocatalyst (n = 1/2 for direct transition and n = 2 for indirect transition). By extrapolating the linear portion of the $(\alpha h\nu)^2$ curve vs $h\nu$, the value of E_g for different photocatalysts were determined. The band gap for BCN, BVO, BVCN-50 were 2.8, 2.5, and 2.6 eV in that order. The optical evidence suggests that BVCN-50 has improved solar light utilization capability as compared to other photocatalysts.

Photoluminescence Spectroscopy. In order to survey the separation efficiency of photogenerated charge carrier[70] and the tendency of electron hole pairs recombination on the surface as well as at the interface of photocatalysts, photoluminescence spectroscopy was done for all photocatalysts at an excitation of 330 nm and depicted in Figure 3b. It is clear from the figure that a substantial decrease in PL intensity takes place while going from BCN to BVO to BVCN series. Higher PL intensity stands for the higher extent of radiative process related to charge pair recombination. The emission intensity of BCN is broad and centered at 465 nm and is attributed to that band to band transition.[24] Similarly, the cases of BVOM, BVOT, and BVOMT show emission intensity at 432 and 530 nm, which was corroborated by earlier reports (Figure S6b). This double band emission[71] is related to the recombination of electron in the V 3d band with the hole in the O 2p band and Bi^{3+} to V center charge transfer, respectively. The same figure also described that the emission peaks are at 469, 464, and 460 nm for BVCN-25, BVCN-50, and BVCN-75, in that order. A significant decrease in PL intensity in the case of BVCN-50

DOI: 10.1021/acs.inorgchem.9b02309
Inorg. Chem. XXXX, XXX, XXX−XXX

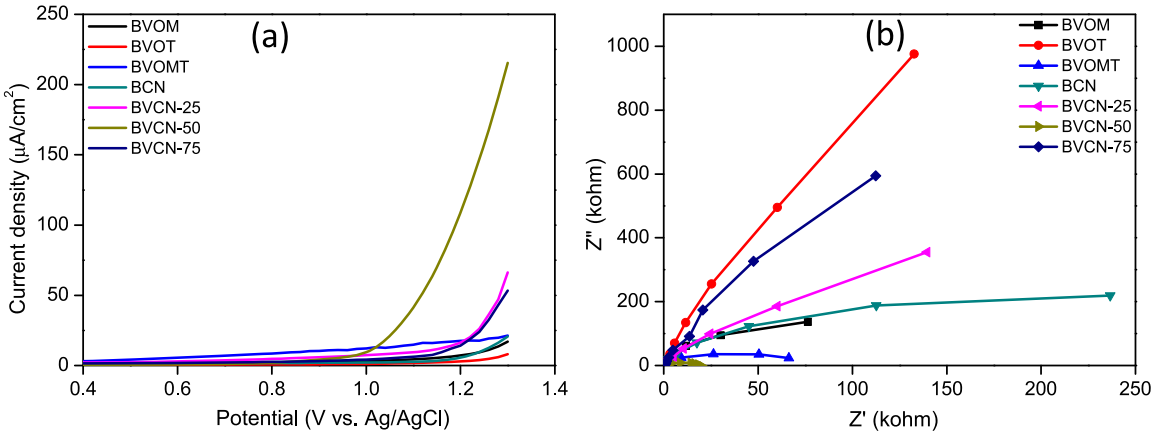

Figure 4. (a) Linear sweep voltammetry and (b) electrochemical impedance spectra of all photocatalysts.

indicates the rate of electron−hole recombination is lowest as compared to others and hence related to the highest photocatalytic activity by BVCN-50.

Photoelectrochemical Properties. Photoelectrochemical analyses of as designed photocatalysts were examined by a standard three electrode system by using 0.2 M Na_2SO_4 solution as electrolyte and depicted in Figure 4a. As expected from a n-type semiconductor,[12] BVO electrode acts as photoanode which generates anodic photocurrent by using the photoinduced holes for water oxidation at the semiconductor-electrolyte interface. All photocatalysts show almost negligible current (nA range) in the dark (Figure S7a). Upon light illumination, BVOM and BCN show 8.7 and 20.4 μA current in anodic direction. The higher photocurrent generation by BCN as compared to BVOM is attributed to the thin nanosheet nature of BCN where electrons are channelized more easily. Since BCN is identified to improve electron transportation in a composite due to the large quantities of delocalized electrons from the conjugated sp^2 hybridized carbon network.[21] Similarly photocurrent generation by BVOT and BVOMT was found to be 8.7 and 20.8 μA. BVCN-25 and BVCN-75 generate 65.7 and 53.4 μA current in the anodic direction upon light irradiation. More interestingly, BVCN-50 shows 215 μA anodic current at a potential of 1 V, and the overpotential[72] decreases up to 0.24 V as compared to other photocatalysts. The abrupt decrease in the overpotential is attributed to the staggered energy band and formation of high quality heterostructures between BVOMT and BCN. The catalyst BVCN-50 shows highest oxygen evolution activities with a strong negative shift in the onset potential, which links to the lower surface recombination.[73] The higher photocurrent relates to the better charge separation efficiency of BVCN-50. The catalyst has more ability for charge separation and generates 30- and 10.5-fold photocurrent as compared to neat BVO and BCN respectively. The highest photocurrent and negative shifting in overpotential relates to the superior photocatalytic activity by BVCN-50. Moreover, the photoelectrochemical reversibility of the electrode was assessed from transient photocurrent response analysis and depicted in Figure S7b. A sharp increment in the photocurrent response was observed upon light illumination, which relapses back to the original state under dark. Among the various photocatalysts examined in this study, BVCN-50 exhibits the highest photocurrent that shows 2.5 times higher than BCN and 3.5-fold higher than BVOM. These photoelectrodes retain excellent reversibility and photostability of the materials.

The interfacial properties between the electrode (BCN, BVOM, BVOT, BVOMT, BVCN-25, BVCN-50, and BVCN-75) and electrolyte were examined by electrochemical impedance spectroscopy[74] measurement. The Nyquist plot generally consists of semicircle[75] (i.e., arch in the present study), where x and y axes represents the real part (Z') and negative of imaginary part (Z''). The semicircle generally represents the charge-transfer process, while the diameter of the semicircle links to the charge transfer resistance. It is well established that the large value of impedance signifies the poor conductivity of electron across the electrode and electrolyte interface.[23] From the Figure 4b, it is clear that the charge transfer resistance for BVOM, BVOT, BVOMT, BCN, BVCN-25, BVCN-50, and BVCN-75 were 76.4, 132.7, 66.2, 113.0, 139.5, 19.1, and 112.5 kΩ respectively. The smallest diameter in case of BVCN-50 is attributed to the lesser charge transfer resistance due to the tremendous electrical conductivity by the material. Again the staggered energy band and formation of high quality heterostructures in case of BVCN-50 are responsible for the excellent electrical conducting nature, which makes it the best photocatalyst among all synthesized materials. Mott−Schottky measurement was implemented in 0.2 M Na_2SO_4 (pH = 6.1) so as to know the band edge potential and type of the semiconductor[76,23] photocatalyst and is depicted in Figure S8. Parts a and b of Figure S8 reveal that straight lines having positive slope is extrapolated to the potential axis in case of both monoclinic and tetragonal phase of BVO, representing the materials to be intrinsic n-type[12] semiconductors. Similarly, a negative slope is drawn to the potential axis for BCN (Figure S8c), which indicate the intrinsic p-type character of the material. The CB position of n-type and VB position of p-type semiconductors were evaluated using following equation.

$$E_{fb(vs.NHE)} = E_{fb(pH=0,vs.Ag/AgCl)} + E_{AgCl} + 0.059\ \mathrm{pH}$$

The CB potential for both monoclinic and tetragonal BVO was +0.3 and −0.1 eV, and for BCN, the VB potential was 2.0 eV. The corresponding VB potential for monoclinic and tetragonal BVO and CB position for BCN were calculated from UV−vis results by means of the equation $E_{VB} = E_g + E_{CB}$. Excitingly, in the case of BVCN-50 (Figure S8d), an inverted U shaped curve is obtained, and both positive and negative slope can be plotted which are located at different potential regimes. This is

DOI: 10.1021/acs.inorgchem.9b02309
Inorg. Chem. XXXX, XXX, XXX−XXX

a symbolic case for the coexistence of together p- and n-type properties in the photocatalyst[23] where a suitable p−n photochemical heterojunction is established at the interface of BVO and BCN. The Fermi level of both p- and n-type domains occurs at the interface, creating a built-in electric field. The built-in electric field is responsible for the migration of photogenerated electrons in opposite directions and improves the separation of electron hole pairs and ultimately triggers the photocatalytic activity.

Photocatalytic Activity. In addition to the application of water in photooxidation, an excellent photocatalyst should simultaneously have a photoreduction ability. The health hazard to both humans and animals is due to the presence of heavy metal ions like Cr(VI) in aquatic bodies causing pollution problems. Here, we have chosen Cr(VI) as a model pollutant for photocatalytic reduction as it is not only carcinogenic and mutagenic to humans but also highly toxic[77] due its mobility in aqueous medium. For the reduction experiment, 50 mg of catalyst was placed in 20 mL (20 ppm, pH = 2, adjusted by adding 0.1 M HCl) of Cr(VI) solution and sonicated for 10 min. The solutions were stirred in the dark for 30 min to attain an equilibrium adsorption state prior to visible light illumination. Blank experiment without photocatalyst reveals the negligible photolysis of Cr(VI) solution under light irradiation. The rate constant for Cr(VI) reduction reaction by all synthesized catalysts are depicted in the Table 1. From

Table 1. First Order Fitting Results of Cr(VI) Reduction over All Photocatalysts

catalyst	R^2	k_{obs} (min^{-1})	$t_{1/2}$ (min)	% of degradation
BVOM	0.998	0.0115	60.26	17
BVOT	0.994	0.0081	85.56	15
BVOMT	0.998	0.0237	29.24	33
BCN	0.999	0.0433	16.01	75
BVCN-25	0.999	0.0469	14.77	78
BVCN-50	0.999	0.0533	13.00	87
BVCN-75	0.998	0.0311	22.28	66

Figure 5a, it is confirmed that after light illumination for 30 min, there was a significant decrease in Cr(VI) concentration for BVOM (17%), BVOT (15%), BVOMT (33%), BCN (72%), BVCN-25 (77%), BVCN-50 (85%), and BVCN-75 (66%). The decrease in photocatalytic activity in case of BVCN-75 is attributed to the presence of large quantity of BVO on the surface of BVCN. A higher percentage of BVO in BVCN-75 retards the light penetration ability of the composite and also restricts the interfacial charge transfer. To explore the kinetics of Cr(VI) reduction, experimental data were fitted with a first order model by using the following formula.

$$\ln(C/C_0) = -kt$$

Here C_0 and C are the initial and final concentration after time t, and k is the rate constant for the reduction reaction. The rate constant follows the order BVOT < BVOM < BVOMT < BVCN-75 < BCN < BVCN-25 < BVCN-50 (Figure 5b). The rate constant for BVCN-50 is 7.9-fold higher than that of BVO. Figure 5c represents the spectral changes of Cr(VI) solution after different time intervals over BVCN-50. The pH of the solution has a significant role for the absorption and reduction of Cr(VI) to Cr(III). In addition to this, the Cr(VI) reduction reaction has been performed in river water where the experimental conditions were kept the same as in the case of distilled water. From Figure S9a,b, it is clear that, after light illumination, the Cr(VI) concentration decreases significantly for BVOM (14%), BVOT (11%), BVOMT (25%), BCN (73%), BVCN-25 (75%), BVCN-50 (80%), and BVCN-75 (60%). The decrease in the percentage of Cr(VI) reduction in river water as compared to distilled water may be attributed to the presence of different ions, which interfere during the adsorption and photoreduction process. The percentage of Cr(VI) reduction in wastewater by the foremost catalyst BVCN-50 was found to be 62%, and the decrease in photocatalytic activity as compared to in distilled and river water medium is attributed to the presence of a large numbers of interfering ions.

The photocatalytic reduction process was found to be decreased upon increasing the pH of the solution.[78] The surface of the photocatalyst was positively charged at lower pH due to protonation and attracts negatively charged $HCrO_4^-$ ions, subsequently facilitating the adsorption process. The same reaction has been performed at different pHs and is depicted in Figure S10a,b, and the highest reduction rate was found at pH = 2. This is attributed to the adsorption of greater numbers of protons on the surface of the photocatalyst, increasing its proton exchange capacity. Upon increase in pH, the $HCrO_4^-$ species is converted to more negatively charged species like CrO_4^{2-} and $Cr_2O_7^{2-}$. Therefore, the reduction rate decreases significantly due to the formation of negatively charged surface, which causes repulsion between the catalyst surface and $HCrO_4^-$ ion and decreases the adsorption rate. So as to know the photostability of the catalyst, repeated experiments were performed with an interval of 40 min and results were shown in Figure S10c.

The photocatalytic water splitting reaction has been achieved in a 100 mL sealed quartz batch reactor and analyzed by gas chromatography under visible light illumination. Both BVOM and BCN were able to generate similar oxygen evolution rates, 321 and 318 μmol $h^{-1}g^{-1}$, respectively, whereas in the case of BVOT and BVOMT. the oxygen production rates were 256 and 452.8 μmol $h^{-1}g^{-1}$(Figure 5d). BVOM has a band gap of 2.4 eV, which is able to absorb visible light, but the photocatalytic water oxidation has been inhibited due to its poor hole mobility. The oxygen evolution rate of BCN is akin to BVOM even though the band gap is 2.8 eV for BCN which links to the better charge mobility.[33,38] The composite heterojunction photocatalyst have improved charge separation and migration which results in enhancement in the photocatalytic activity. The oxygen evolution rate of BVCN-25, BVCN-50, and BVCN-75 were 1027.2, 1348.2, and 898.8 μmol h^{-1} g^{-1}. The oxygen evolution activity by BVCN-50 is 4.2 times higher than that of BVO whereas photocatalytic activity decreases in case of BVCN-75. Repeated experiments were performed in order to know the photostability of the catalyst with an interval of 3 h and depicted in Figure S10d. After reusability test of the photocatalyst, the crystal structure and morphology of BVCN-50 remain intact as revealed from PXRD (Figure S11) and FESEM image (Figure S12). Decrease in the photocatalytic activity by BVCN-75 is attributed to agglomeration of BVO due to its higher content that causes blocking of light. Therefore, BVCN-50 is regarded as a saturated composite catalyst between BVO and BCN. For comparative study, various BVO-based p−n heterojunction photocatalysts and their activities were tabulated (Table S1).

Mechanism. The improved photocatalytic activity of the heterostructure can be described by assuming the formation of

DOI: 10.1021/acs.inorgchem.9b02309
Inorg. Chem. XXXX, XXX, XXX−XXX

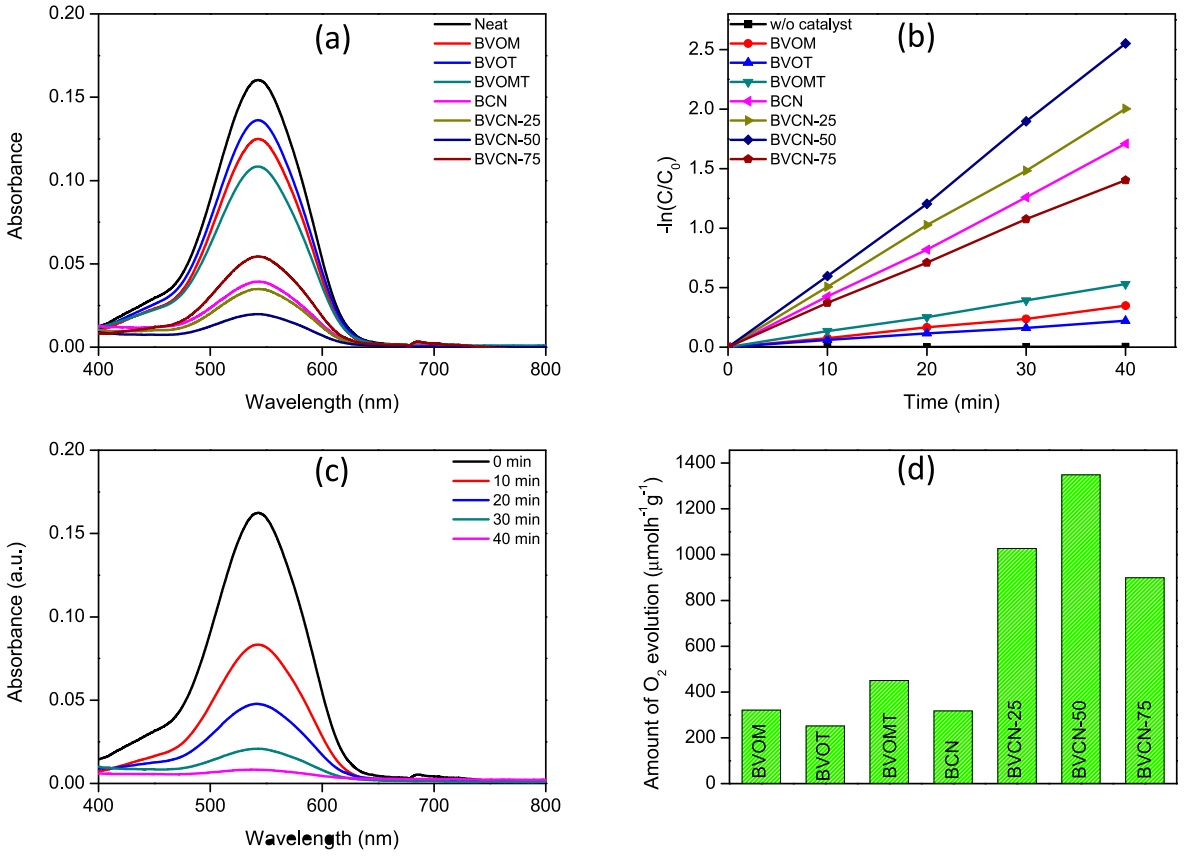

Figure 5. (a) UV−vis spectra of Cr(VI) reduction over all synthesized photocatalysts. (b) First order kinetics plot. (c) spectral changes of Cr(VI) solution after different time interval over BVCN-50. (d) Photocatalytic oxygen evolution by all synthesized photocatalysts.

p−n heterojunction. In order to study the type of semiconductor, Mott−Schottky analysis was performed, and from Figure S8, it is confirmed that the slope of the linear $1/C^2$ potential curve of BVO and BCN were positive and negative. The results demonstrate that BCN has an intrinsic p-type[33] characteristic whereas BVO an intrinsic n-type.[12] The Fermi level (E_F) of BCN (p-type) remains close to the VB, and for BVO (n-type), the Fermi level (E_F) is close to CB.[79] When BVO is assembled on to the BCN surface (Scheme S1), a type-II p−n heterojunction is formed. In order to established equilibrium in the E_F value of both semiconductors[80] forming p−n heterojunction, the energy levels of BVO move downward and energy levels of BCN shift upward. Ultimately, the conduction band edge potential of BVO is lower as compared to BCN. Upon visible light irradiation, both BVO and BCN in BVCN heterostructure could simultaneously be excited to form electron−hole pairs. Alongside this, the internal electric field is also responsible for the improvement in the immigration of photoinduced charge carriers. Due to the presence of both monoclinic and tetragonal phase, the photoinduced electrons from the CB of tetragaonal phase can easily channelized in to the CB of monoclinic phase facilitating reduction reaction. Consequently, the BVCN p−n heterojunction not only promotes the separation of the photoinduced electron−hole pairs but also reduces the recombination of charge carriers, thus enhancing its photocatalytic activity. The excited electron can easily migrate from the CB of BCN to the CB of BVO where it reduces Cr(VI) to Cr(III). Simultaneously holes get transferred from VB of BVO to the VB of BCN and oxidize H_2O to O_2 (Scheme 2). The molecular reaction mechanism is summarized below.

$$BVCN + h\nu \rightarrow BVCN(e_{CB}^{-} + h_{VB}^{+})$$

$$BVCN(e_{CB}^{-}) + Cr(VI) \rightarrow Cr(III)$$

$$BVCN(h_{VB}^{+}) + 2H_2O \rightarrow O_2 + 4H^{+}$$

CONCLUSION

Graphitic-like boron-doped g-C_3N_4 nanosheet was fabricated and $BiVO_4$ nanostructure deposited on to it to construct p−n heterojunction photocatalyst for effective simultaneous reduction of Cr(VI) and oxidation of H_2O to generate O_2.

Scheme 2. Plausible Mechanism for Photocatalytic Cr(VI) Reduction and Oxygen Evolution on BVCN-50

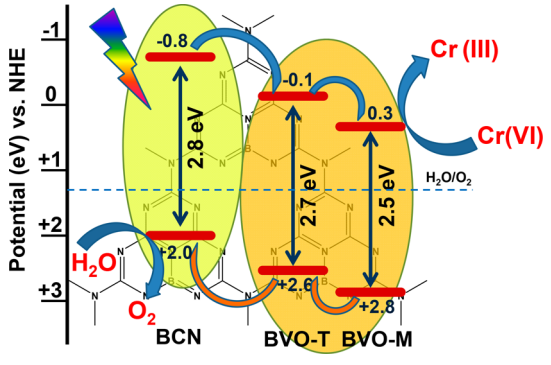

DOI: 10.1021/acs.inorgchem.9b02309
Inorg. Chem. XXXX, XXX, XXX−XXX

Monoclinic and tetragonal mixed phase $BiVO_4$ is obtained due to thermal calcination of the catalyst at 400 °C as well as surface energy of BCN and confirmed from PXRD and HRTEM data. The best photocatalytic activity of 50% $BiVO_4$/B-doped g-C_3N_4 for the reduction of Cr(VI) is 3.9-fold higher than that of $BiVO_4$. Again the photocatalyst is able to generate 4.2 times higher oxygen evolution rate as compared to $BiVO_4$. The excellent enhancement in the photocatalytic activity of $BiVO_4$/B-doped g-C_3N_4 is ascribed to its strong absorption of visible light and low recombination rate of electron−hole pairs due to the formation of type-II p−n heterojunction between $BiVO_4$ and B-doped g-C_3N_4. The built in electrostatic field at the junction is also responsible for the generation of excellent photocurrent by the heterojunction as compared to neat material. The results were corroborated by UV−vis, PL, photocurrent response, and electrochemical impedance spectroscopy. Moreover oxygen vacancy in the photocatalyst is also accountable for the excellent photocatalytic activity by the heterostructure and is validated from XPS and Raman analysis. The photocatalyst also exhibits excellent photostability and recyclability. The present work validates a facile way for the construction of p−n heterojunctions with improved visible light driven photocatalytic properties.

■ ASSOCIATED CONTENT

Supporting Information

The Supporting Information is available free of charge on the ACS Publications website at DOI: 10.1021/acs.inorgchem.9b02309.

FTIR, Raman, FESEM, and EDS, elemental mapping of BVCN-50, surface area of BVOMT, BCN, and BVCN-50, XPS spectra of BCN, Tauc's plot and Pl spectra of all photocatalysts, current density in dark and transient photocurrent density, Mott−Schottky plot, UV−vis spectra of Cr(VI) reduction and first order kinetics plot in river water, effect of pH on Cr(VI) reduction, reusability curve of Cr(VI) reduction and photocatalytic O_2 evolution, PXRD plot and FESEM plot after reusability test, literature survey based on various p−n heterojunctions, formation mechanism of p−n heterojunctions, and probable charge separation process in BVCN heterostructure (PDF)

■ AUTHOR INFORMATION

Corresponding Authors

*(B.N.) E-mail: brundabananaik@soa.ac.in.

*(K.P.) E-mail: kulamaniparida@soa.ac.in; paridakulamani@yahoo.com.

ORCID

Pradeepta Babu: 0000-0001-5457-4307

Satyaranjan Mohanty: 0000-0002-1603-6812

Brundabana Naik: 0000-0001-5568-1171

Kulamani Parida: 0000-0001-7807-5561

Notes

The authors declare no competing financial interest.

■ ACKNOWLEDGMENTS

All the authors are very much thankful to Siksha 'O' Anusandhan, Bhubaneswar, India, for infrastructure. K.P. and P.B. acknowledge SERB, India (EMR/2016/000606) for funding and fellowship, respectively. S.M. acknowledges Siksha 'O' Anusandhan, Bhubaneswar, India for a fellowship.

■ REFERENCES

(1) Hoffmann, M. R.; Martin, S. T.; Choi, W.; Bahnemann, D. W. Environmental applications of semiconductor photocatalysis. *Chem. Rev.* **1995**, *95* (1), 69−96.

(2) Serpone, N.; Emeline, A. V. Semiconductor photocatalysis — past, present, and future outlook. *J. Phys. Chem. Lett.* **2012**, *3* (5), 673−677.

(3) Moniz, S. J. A.; Shevlin, S. A.; Martin, D. J.; Guo, Z.-X.; Tang, J. Visible-light driven heterojunctionphotocatalysts for water splitting − a critical review. *Energy Environ. Sci.* **2015**, *8* (3), 731−759.

(4) Wang, H.; Zhang, L.; Chen, Z.; Hu, J.; Li, S.; Wang, Z.; Liu, J.; Wang, X. Semiconductor heterojunctionphotocatalysts: design, construction, and photocatalytic performances. *Chem. Soc. Rev.* **2014**, *43* (15), 5234−5244.

(5) Naik, B.; Parida, K. M.; Gopinath, C. S. Facile Synthesis of N- and S-incorporated nanocrystallineTiO_2 and direct solar-light-driven photocatalytic activity. *J. Phys. Chem. C* **2010**, *114* (45), 19473−19482.

(6) Mohanty, S.; Babu, P.; Parida, K.; Naik, B. Surface-Plasmon-Resonance-Induced Photocatalysis by Core-Shell SiO_2@ Ag NCs@ Ag_3PO_4 toward Water-Splitting and Phenol Oxidation Reactions. *Inorg. Chem.* **2019**, *58*, 9643.

(7) Patnaik, S.; Martha, S.; Parida, K. M. An overview of the structural, textural and morphological modulations of g-C_3N_4 towards photocatalytic hydrogen production. *RSC Adv.* **2016**, *6* (52), 46929−46951.

(8) Abdi, F. F.; Han, L.; Smets, A. H.; Zeman, M.; Dam, B.; Van De Krol, R. Efficient solar water splitting by enhanced charge separation in a bismuth vanadate-silicon tandem photoelectrode. *Nat. Commun.* **2013**, *4*, 2195.

(9) Seabold, J. A.; Choi, K. S. Efficient and stable photo-oxidation of water by a bismuth vanadate photoanode coupled with an iron oxyhydroxide oxygen evolution catalyst. *J. Am. Chem. Soc.* **2012**, *134* (4), 2186−2192.

(10) Tokunaga, S.; Kato, H.; Kudo, A. Selective preparation of monoclinic and tetragonal $BiVO_4$ with scheelite structure and their photocatalytic properties. *Chem. Mater.* **2001**, *13* (12), 4624−4628.

(11) Xi, G.; Ye, J. Synthesis of bismuth vanadate nanoplates with exposed {001} facets and enhanced visible-light photocatalytic properties. *Chem. Commun.* **2010**, *46* (11), 1893−1895.

(12) Park, Y.; McDonald, K. J.; Choi, K.-S. Progress in bismuth vanadate photoanodes for use in solar water oxidation. *Chem. Soc. Rev.* **2013**, *42* (6), 2321−2337.

(13) Kweon, K. E.; Hwang, G. S. Structural phase-dependent hole localization and transport in bismuth vanadate. *Phys. Rev. B: Condens. Matter Mater. Phys.* **2013**, *87* (20), 205202.

(14) Hong, S. J.; Lee, S.; Jang, J. S.; Lee, J. S. Heterojunction $BiVO_4$/WO_3 electrodes for enhanced photoactivity of water oxidation. *Energy Environ. Sci.* **2011**, *4* (5), 1781−1787.

(15) Long, M.; Cai, W.; Kisch, H. Visible Light Induced Photoelectrochemical Properties of n-$BiVO_4$ and n-$BiVO_4$/p-Co_3O_4. *J. Phys. Chem. C* **2008**, *112* (2), 548−554.

(16) Cao, S.-W.; Yin, Z.; Barber, J.; Boey, F. Y.; Loo, S. C. J.; Xue, C. Preparation of Au-$BiVO_4$ heterogeneous nanostructures as highly efficient visible-light photocatalysts. *ACS Appl. Mater. Interfaces* **2012**, *4* (1), 418−423.

(17) Jo, W. J.; Jang, J. W.; Kong, K. j.; Kang, H. J.; Kim, J. Y.; Jun, H.; Parmar, K.; Lee, J. S. Phosphate doping into monoclinic $BiVO_4$ for enhanced photoelectrochemical water oxidation activity. *Angew. Chem.* **2012**, *124* (13), 3201−3205.

(18) Cheng, J.; Feng, J.; Pan, W. Enhanced photocatalytic activity in electrospun bismuth vanadate nanofibers with phase junction. *ACS Appl. Mater. Interfaces* **2015**, *7* (18), 9638−9644.

(19) Fan, H.; Jiang, T.; Li, H.; Wang, D.; Wang, L.; Zhai, J.; He, D.; Wang, P.; Xie, T. Effect of $BiVO_4$ crystalline phases on the

DOI: 10.1021/acs.inorgchem.9b02309
Inorg. Chem. XXXX, XXX, XXX−XXX

photoinduced carriers behavior and photocatalytic activity. *J. Phys. Chem. C* **2012**, *116* (3), 2425−2430.
(20) Tan, G.; Zhang, L.; Ren, H.; Wei, S.; Huang, J.; Xia, A. Effects of pH on the hierarchical structures and photocatalytic performance of $BiVO_4$ powders prepared via the microwave hydrothermal method. *ACS Appl. Mater. Interfaces* **2013**, *5* (11), 5186−5193.
(21) Cao, S.; Low, J.; Yu, J.; Jaroniec, M. Polymeric photocatalysts based on graphitic carbon nitride. *Adv. Mater.* **2015**, *27* (13), 2150−2176.
(22) Wang, X.; Blechert, S.; Antonietti, M. Polymeric graphitic carbon nitride for heterogeneous photocatalysis. *ACS Catal.* **2012**, *2* (8), 1596−1606.
(23) Babu, P.; Mohanty, S.; Naik, B.; Parida, K. Synergistic effects of boron and sulfur co-doping into graphitic carbon nitride framework for enhanced photocatalytic activity in visible light driven hydrogen generation. *ACS Applied Energy Materials* **2018**, *1* (11), 5936−5947.
(24) Martha, S.; Nashim, A.; Parida, K. M. Facile synthesis of highly active g-C_3N_4 for efficient hydrogen production under visible light. *J. Mater. Chem. A* **2013**, *1* (26), 7816−7824.
(25) Cui, L.; Song, J.; McGuire, A. F.; Kang, S.; Fang, X.; Wang, J.; Yin, C.; Li, X.; Wang, Y.; Cui, B. Constructing highly uniform onion-ring-like graphitic carbon nitride for efficient visible-light-driven photocatalytic hydrogen evolution. *ACS Nano* **2018**, *12* (6), 5551−5558.
(26) Mo, Z.; Xu, H.; Chen, Z.; She, X.; Song, Y.; Wu, J.; Yan, P.; Xu, L.; Lei, Y.; Yuan, S.; et al. Self-assembled synthesis of defect-engineered graphitic carbon nitride nanotubes for efficient conversion of solar energy. *Appl. Catal., B* **2018**, *225*, 154−161.
(27) Liang, Q.; Li, Z.; Huang, Z. H.; Kang, F.; Yang, Q. H. Holey graphitic carbon nitride nanosheets with carbon vacancies for highly improved photocatalytic hydrogen production. *Adv. Funct. Mater.* **2015**, *25* (44), 6885−6892.
(28) Ye, M. Y.; Zhao, Z. H.; Hu, Z. F.; Liu, L. Q.; Ji, H. M.; Shen, Z. R.; Ma, T. Y. 0D/2D heterojunctions of vanadate quantum dots/graphitic carbon nitride nanosheets for enhanced visible light driven photocatalysis. *Angew. Chem., Int. Ed.* **2017**, *56* (29), 8407−8411.
(29) Han, Y. Y.; Lu, X. L.; Tang, S. F.; Yin, X. P.; Wei, Z. W.; Lu, T. B. Metal free 2D/2D heterojunction of graphitic carbon nitride/graphdiyne for improving the hole mobility of graphitic carbon nitride. *Adv. Energy Mater.* **2018**, *8* (16), 1702992.
(30) Hu, S.; Li, F.; Fan, Z.; Wang, F.; Zhao, Y.; Lv, Z. Band gap-tunable potassium doped graphitic carbon nitride with enhanced mineralization ability. *Dalton Trans* **2015**, *44* (3), 1084−1092.
(31) Zhang, M.; Bai, X.; Liu, D.; Wang, J.; Zhu, Y. Enhanced catalytic activity of potassium-doped graphitic carbon nitride induced by lower valence position. *Appl. Catal., B* **2015**, *164*, 77−81.
(32) Zhang, Y.; Mori, T.; Ye, J.; Antonietti, M. Phosphorus-doped carbon nitride solid: enhanced electrical conductivity and photocurrent generation. *J. Am. Chem. Soc.* **2010**, *132* (18), 6294−6295.
(33) Thaweesak, S.; Wang, S.; Lyu, M.; Xiao, M.; Peerakiatkhajohn, P.; Wang, L. Boron-doped graphitic carbon nitride nanosheets for enhanced visible light photocatalytic water splitting. *Dalton Tran* **2017**, *46* (32), 10714−10720.
(34) Li, C.; Wang, S.; Wang, T.; Wei, Y.; Zhang, P.; Gong, J. Monoclinic porous $BiVO_4$ networks decorated by discrete g-C_3N_4 nanoislands with tunable coverage for highly efficient photocatalysis. *Small* **2014**, *10* (14), 2783−2790.
(35) Samanta, S.; Khilari, S.; Pradhan, D.; Srivastava, R. An efficient, visible light driven, selective oxidation of aromatic alcohols and amines with O_2 using $BiVO_4$/g-C_3N_4 nanocomposite: a systematic and comprehensive study toward the development of a photocatalytic process. *ACS Sustainable Chem. Eng.* **2017**, *5* (3), 2562−2577.
(36) Sun, R.; Shi, Q.; Zhang, M.; Xie, L.; Chen, J.; Yang, X.; Chen, M.; Zhao, W. Enhanced photocatalytic oxidation of toluene with a coral-like direct Z-scheme $BiVO_4$/g-C_3N_4 photocatalyst. *J. Alloys Compd.* **2017**, *714*, 619−626.
(37) Wang, Y.; Sun, J.; Li, J.; Zhao, X. Electrospinning preparation of nanostructured g-C_3N_4/$BiVO_4$ composite films with an enhanced photoelectrochemical performance. *Langmuir* **2017**, *33* (19), 4694−4701.
(38) Kong, H. J.; Won, D. H.; Kim, J.; Woo, S. I. Sulfur-Doped g-C_3N_4/$BiVO_4$ Composite Photocatalyst for Water Oxidation under Visible Light. *Chem. Mater.* **2016**, *28* (5), 1318−1324.
(39) Wu, Y.; Wang, H.; Tu, W.; Liu, Y.; Tan, Y. Z.; Yuan, X.; Chew, J. W. Quasi-polymeric construction of stable perovskite-type $LaFeO_3$/g-C_3N_4 heterostructuredphotocatalyst for improved Z-scheme photocatalytic activity via solid p−n heterojunction interfacial effect. *J. Hazard. Mater.* **2018**, *347*, 412−422.
(40) Wang, H.; Wu, Y.; Feng, M.; Tu, W.; Xiao, T.; Xiong, T.; Ang, H.; Yuan, X.; Chew, J. W. Visible-light-driven removal of tetracycline antibiotics and reclamation of hydrogen energy from natural water matrices and wastewater by polymeric carbon nitride foam. *Water Res.* **2018**, *144*, 215−225.
(41) Wu, Y.; Wang, H.; Sun, Y.; Xiao, T.; Tu, W.; Yuan, X.; Zeng, G.; Li, S.; Chew, J. W. Photogenerated charge transfer via interfacial internal electric field for significantly improved photocatalysis in direct Z-scheme oxygen-doped carbon nitrogen/CoAl-layered double hydroxide heterojunction. *Appl. Catal., B* **2018**, *227*, 530−540.
(42) Wu, Y.; Wang, H.; Tu, W.; Wu, S.; Liu, Y.; Tan, Y. Z.; Luo, H.; Yuan, X.; Chew, J. W. Petal-like CdS nanostructures coated with exfoliated sulfur-doped carbon nitride via chemically activated chain termination for enhanced visible light driven photocatalytic water purification and H_2 generation. *Appl. Catal., B* **2018**, *229*, 181−191.
(43) Wu, Y.; Wang, H.; Tu, W.; Liu, Y.; Wu, S.; Tan, Y. Z.; Chew, J. W. Construction of hierarchical 2D-2D $Zn_3In_2S_6$/fluorinated polymeric carbon nitride nanosheetsphotocatalyst for boosting photocatalytic degradation and hydrogen production performance. *Appl. Catal., B* **2018**, *233*, 58−69.
(44) Yu, J.; Zhang, Y.; Kudo, A. Synthesis and photocatalytic performances of $BiVO_4$ by ammonia co-precipitation process. *J. Solid State Chem.* **2009**, *182* (2), 223−228.
(45) Baral, B.; Reddy, K. H.; Parida, K. M. Construction of M-$BiVO_4$/T-$BiVO_4$ isotypeheterojunction for enhanced photocatalytic degradation of Norfloxacine and Oxygen evolution reaction. *J. Colloid Interface Sci.* **2019**, *554*, 278.
(46) Ng, Y. H.; Iwase, A.; Kudo, A.; Amal, R. Reducing Graphene Oxide on a Visible-Light $BiVO_4$Photocatalyst for an Enhanced Photoelectrochemical Water Splitting. *J. Phys. Chem. Lett.* **2010**, *1* (17), 2607−2612.
(47) Wang, W.; Lai, M.; Fang, J.; Lu, C. Au andPt selectively deposited on {001}-faceted TiO_2 toward SPR enhanced photocatalytic Cr(VI) reduction: The influence of excitation wavelength. *Appl. Surf. Sci.* **2018**, *439*, 430−438.
(48) Samantaray, S. K.; Mohapatra, P.; Parida, K. Physico-chemical characterisation and photocatalytic activity of nanosized SO_4^{2-}/TiO_2 towards degradation of 4-nitrophenol. *J. Mol. Catal. A: Chem.* **2003**, *198* (1−2), 277−287.
(49) Fina, F.; Callear, S. K.; Carins, G. M.; Irvine, J. T. Structural investigation of graphitic carbon nitride via XRD and neutron diffraction. *Chem. Mater.* **2015**, *27* (7), 2612−2618.
(50) Zhou, D.; Pang, L.-X.; Guo, J.; Qi, Z.-M.; Shao, T.; Wang, Q.-P.; Xie, H.-D.; Yao, X.; Randall, C. A. Influence of Ce Substitution for Bi in $BiVO_4$ and the Impact on the Phase Evolution and Microwave Dielectric Properties. *Inorg. Chem.* **2014**, *53* (2), 1048−1055.
(51) Zhang, H. M.; Liu, J. B.; Wang, H.; Zhang, W. X.; Yan, H. Rapid microwave-assisted synthesis of phase controlled $BiVO_4$ nanocrystals and research on photocatalytic properties under visible light irradiation. *J. Nanopart. Res.* **2008**, *10* (5), 767−774.
(52) Li, X.; Qi, W.; Mei, D.; Sushko, M. L.; Aksay, I.; Liu, J. Functionalized Graphene Sheets as Molecular Templates for Controlled Nucleation and Self Assembly of Metal Oxide GrapheneNanocomposites. *Adv. Mater.* **2012**, *24* (37), 5136−5141.
(53) Guo, H.; Dong, N.; Yin, M.; Zhang, W.; Lou, L.; Xia, S. Visible upconversion in rare earth ion-doped Gd_2O_3 nanocrystals. *J. Phys. Chem. B* **2004**, *108* (50), 19205−19209.
(54) Sun, J.; Chen, G.; Wu, J.; Dong, H.; Xiong, G. Bismuth vanadate hollow spheres: Bubble template synthesis and enhanced

DOI: 10.1021/acs.inorgchem.9b02309
Inorg. Chem. XXXX, XXX, XXX−XXX

photocatalytic properties for photodegradation. *Appl. Catal., B* **2013**, *132*, 304−314.
(55) Liu, S.; Yin, K.; Ren, W.; Cheng, B.; Yu, J. Tandem photocatalytic oxidation of Rhodamine B over surface fluorinated bismuth vanadate crystals. *J. Mater. Chem.* **2012**, *22* (34), 17759−17767.
(56) Frost, R. L.; Henry, D. A.; Weier, M. L.; Martens, W. Raman spectroscopy of three polymorphs of $BiVO_4$: clinobisvanite, dreyerite and pucherite, with comparisons to $(VO_4)^{3-}$ bearing minerals: namibite, pottsite and schumacherite. *J. Raman Spectrosc.* **2006**, *37* (7), 722−732.
(57) Nikam, S.; Joshi, S. Irreversible phase transition in $BiVO_4$ nanostructures synthesized by a polyol method and enhancement in photo degradation of methylene blue. *RSC Adv.* **2016**, *6* (109), 107463−107474.
(58) Merupo, V.-I.; Velumani, S.; Ordon, K.; Errien, N.; Szade, J.; Kassiba, A.-H. Structural and optical characterization of ball-milled copper-doped bismuth vanadium oxide ($BiVO_4$). *CrystEngComm* **2015**, *17* (17), 3366−3375.
(59) Chen, L.; Alarcón-Lladó, E.; Hettick, M.; Sharp, I. D.; Lin, Y.; Javey, A.; Ager, J. W. Reactive sputtering of bismuth vanadate photoanodes for solar water splitting. *J. Phys. Chem. C* **2013**, *117* (42), 21635−21642.
(60) Xin, Y.; Zhao, Y.; Qiu, B.; Zhang, Z. Sputtering gold nanoparticles on nanoporous bismuth vanadate for sensitive and selective photoelectrochemicalaptasensing of thrombin. *Chem. Commun.* **2017**, *53* (63), 8898−8901.
(61) Dian, J.; Macek, A.; Nižňanský, D.; Němec, I.; Vrkoslav, V.; Chvojka, T.; Jelınek, I. SEM and HRTEM study of porous silicon—relationship between fabrication, morphology and optical properties. *Appl. Surf. Sci.* **2004**, *238* (1−4), 169−174.
(62) Xie, B. Q.; Qian, Y.; Zhang, S.; Fu, S.; Yu, W. A hydrothermal reduction route to single crystalline hexagonal cobalt nanowires. *Eur. J. Inorg. Chem.* **2006**, *2006* (12), 2454−2459.
(63) Yang, S.; Gong, Y.; Zhang, J.; Zhan, L.; Ma, L.; Fang, Z.; Vajtai, R.; Wang, X.; Ajayan, P. M. Exfoliated graphitic carbon nitride nanosheets as efficient catalysts for hydrogen evolution under visible light. *Adv. Mater.* **2013**, *25* (17), 2452−2456.
(64) Jiang, L.; Yuan, X.; Zeng, G.; Chen, X.; Wu, Z.; Liang, J.; Zhang, J.; Wang, H.; Wang, H. Phosphorus- and sulfur-codopedg-C_3N_4: facile preparation, mechanism insight, and application as efficient photocatalyst for tetracycline and methyl orange degradation under visible light irradiation. *ACS Sustainable Chem. Eng.* **2017**, *5* (7), 5831−5841.
(65) Dong, F.; Zhao, Z.; Xiong, T.; Ni, Z.; Zhang, W.; Sun, Y.; Ho, W.-K. In situ construction of g-C_3N_4/g-C_3N_4 metal-free heterojunction for enhanced visible-light photocatalysis. *ACS Appl. Mater. Interfaces* **2013**, *5* (21), 11392−11401.
(66) Kim, T. W.; Ping, Y.; Galli, G. A.; Choi, K.-S. Simultaneous enhancements in photon absorption and charge transport of bismuth vanadate photoanodes for solar water splitting. *Nat. Commun.* **2015**, *6*, 8769.
(67) Zong, L.; Cui, P.; Qin, F.; Zhao, K.; Wang, Z.; Yu, R. Heterostructured bismuth vanadate multi-shell hollow spheres with high visible-light-driven photocatalytic activity. *Mater. Res. Bull.* **2017**, *86*, 44−50.
(68) Kudo, A.; Omori, K.; Kato, H. A novel aqueous process for preparation of crystal form-controlled and highly crystalline $BiVO_4$ powder from layered vanadates at room temperature and its photocatalytic and photophysical properties. *J. Am. Chem. Soc.* **1999**, *121* (49), 11459−11467.
(69) Sayama, K.; Nomura, A.; Arai, T.; Sugita, T.; Abe, R.; Yanagida, M.; Oi, T.; Iwasaki, Y.; Abe, Y.; Sugihara, H. Photoelectrochemical decomposition of water into H_2 and O_2 on porous $BiVO_4$ thin-film electrodes under visible light and significant effect of Ag ion treatment. *J. Phys. Chem. B* **2006**, *110* (23), 11352−11360.
(70) Rajh, T.; Micic, O. I.; Lawless, D.; Serpone, N. Semiconductor photophysics. 7. Photoluminescence and picosecond charge carrier dynamics in cadmium sulfide quantum dots confined in a silicate glass. *J. Phys. Chem.* **1992**, *96* (11), 4633−4641.
(71) Usai, S.; Obregón, S.; Becerro, A. I.; Colón, G. Monoclinic−Tetragonal Heterostructured $BiVO_4$ by Yttrium Doping with Improved Photocatalytic Activity. *J. Phys. Chem. C* **2013**, *117* (46), 24479−24484.
(72) Yang, J.; Wang, D.; Zhou, X.; Li, C. A theoretical study on the mechanism of photocatalytic oxygen evolution on $BiVO_4$ in aqueous solution. *Chem. - Eur. J.* **2013**, *19* (4), 1320−1326.
(73) Zhong, D. K.; Choi, S.; Gamelin, D. R. Near-complete suppression of surface recombination in solar photoelectrolysis by "Co-Pi" catalyst-modified W: $BiVO_4$. *J. Am. Chem. Soc.* **2011**, *133* (45), 18370−18377.
(74) Park, S. M.; Yoo, J.-S. Peer Reviewed: Electrochemical Impedance Spectroscopy for Better Electrochemical Measurements. *Anal. Chem.* **2003**, *75*, 455A−461A.
(75) García-Jareño, J. J.; Benito, D.; Sanmatías, A.; Vicente, F. Simulation of Impedance Spectra: A Computational and Electrochemical Exercise for University Students. *J. Chem. Educ.* **2000**, *77* (6), 738.
(76) Gelderman, K.; Lee, L.; Donne, S. Flat-band potential of a semiconductor: using the Mott−Schottky equation. *J. Chem. Educ.* **2007**, *84* (4), 685.
(77) Costa, M.; Klein, C. B. Toxicity and carcinogenicity of chromium compounds in humans. *Crit. Rev. Toxicol.* **2006**, *36* (2), 155−163.
(78) Patnaik, S.; Swain, G.; Parida, K. Highly efficient charge transfer through a double Z-scheme mechanism by a Cu-promoted MoO_3/g-C_3N_4 hybrid nanocomposite with superior electrochemical and photocatalytic performance. *Nanoscale* **2018**, *10* (13), 5950−5964.
(79) Huang, H.; He, Y.; Du, X.; Chu, P. K.; Zhang, Y. A general and facile approach to heterostructured core/shell $BiVO_4$/BiOI p−n junction: room-temperature in situ assembly and highly boosted visible-light photocatalysis. *ACS Sustainable Chem. Eng.* **2015**, *3* (12), 3262−3273.
(80) Low, J.; Yu, J.; Jaroniec, M.; Wageh, S.; Al Ghamdi, A. A. Heterojunctionphotocatalysts. *Adv. Mater.* **2017**, *29* (20), 1601694.

DOI: 10.1021/acs.inorgchem.9b02309
Inorg. Chem. XXXX, XXX, XXX−XXX